Title

Integrated simulation of vertical fracture propagation induced by water injection and its borehole electromagnetic responses in shale gas systems

Authors

Kim, Jihoon
Um, Evan Schankee
Moridis, George J

Publication Date

2018-06-01

DOI

10.1016/j.petrol.2018.01.024

Peer reviewed

Integrated simulation of vertical fracture propagation induced by water injection and its borehole electromagnetic responses in shale gas systems

Jihoon Kim[a,b], Evan S. Um[b], George J. Moridis[a,b]

[a]*Harold Vance Department of Petroleum Engineering, Texas A&M University. 3116 TAMU Richardson Building College Station, TX 77843, USA*

[b]*Earth Sciences Division, Lawrence Berkeley National Laboratory. 1 Cyclotron Road 90R1116, Berkeley, CA 94720, USA*

Abstract

We analyze fracture propagation induced by hydraulic fracturing with water injection and examine their detectability with crosswell electromagnetic (EM) geophysical methods. For rigorous 3D coupled flow-geomechanical modeling, we employ a numerical method that can model failure by tensile and shear stresses, dynamic nonlinear permeability, dual continuum approach, and thermo-poro-mechanical effects. From numerical simulation, we find that the fracture propagation is not the same as propagation of the water front, because fracturing is governed by geomechanics whereas water saturation is determined by multiphase flow. At early times, the water front is almost identical to the fracture tip, suggesting that the fracture is mostly filled with the injected water. However, at late times, movement of the water front is retarded compared to fracture propagation, yielding a significant gap between the water front and the fracture top, filled with reservoir gas. During fracture propagation, the coupled flow-geomechnical models are transformed via a rock-physics model into electrical conductivity models. We employ a full 3D finite-element EM geophysical simulator to evaluate the sensitivity of the crosswell EM method to fracture propagation. It is shown that anomalous distribution of electrical conductivity is closely related to the injected water saturation, but not closely related to newly created unsaturated fractures. Our numerical modeling experiments demonstrate that the crosswell EM method can be highly sensitive to electrical conductivity changes that directly indicate the migration pathways of the injected fluid. Accordingly, the EM method can serve as an effective monitoring tool for monitoring the injected fluids during hydraulic fracturing operations.

Keywords: Hydraulic fracturing, Shale gas, Electromagnetic geophysics, Coupled flow and geomechanics

Email addresses: jihoon.kim@tamu.edu (Jihoon Kim), evanum@lbl.gov (Evan S. Um), GJMoridis@lbl.gov (George J. Moridis)

1. Introduction

Hydraulic fracturing with multiple horizontal wells has been widely used in stimulating abundant shale gas reservoirs in order to increase reservoir permeability and productivity (Zoback, 2007; Fjaer et al., 2008; Fisher and Warpinski, 2012; Zoback et al., 2010; Cipolla et al., 2010). Creation of fractures increases the permeability of geological formations by several orders, which can make gas production from very low-permeable reservoirs-such as tight gas and shale gas reservoirs-economically feasible. After the recent success in developing the Barnett shale, other shale gas, such as the Marcellus, Eagle Ford, Haynesville, New Albany, Antrim, and Fayetteville shales in the United States, have been considered as potential resources in the near future. Massive hydraulic fracturing with multiple stage stimulation can significantly enhance reservoir permeability, followed by enhanced productivity and increased stimulated rock volume (SRV) (Kargbo et al., 2010; Arthur and Layne, 2008).

On the other hand, environmental scientists have raised a number of issues related to the environmental impact of hydraulic fracturing, including unstable growth of hydraulic fractures, groundwater contamination, and induced seismicity from fault activation. For example, by performing isotope analysis, Osborn et al. (2011) claimed that methane dissolved in groundwater originated from shale gas reservoirs. Geomechanical failure along the well casing due to incomplete cementing could also be a problem, in that it would create a potential pathway for methane from reservoirs to drinking water aquifers (Zoback et al., 2010). Reservoir engineers, however, argue that the environmental impact of such activity is still limited. For example, according to Fisher and Warpinski (2012), the lengths and tips of hydraulic fractures based on measured microseismic data are finite, being far below drinking-water zones. Also, Rutqvist et al. (2013) showed by using numerical simulation that the magnitudes of induced seismicity caused by fault activation was far below the level discernible by humans.

Many studies in simulating fracture propagation have been done on hydraulic fracturing for several decades, in order to estimate SRV and the lengths of the created fractures, mainly based on 2D or pseudo 3D (Perkins and Kern, 1961; Nordren, 1972; Adachi et al., 2007). Even though such models can provide numerical efficiency and reduce computational cost, full coupling in 3D between flow and geomechanics is required for rigorous modeling of fracture propagation and more reliable risk assessment. Recently, Ji et al. (2009) and Dean and Schmidt (2009) performed numerical modeling of full 3D hydraulic fracturing in the context of coupled flow and geomechanics. Furthermore, Kim and Moridis (2013) extended their modeling, accounting for the dual

continuum model as well as simultaneous tensile and shear failure.

Hydraulic fracturing is typically based on water injection, in which water is mixed with some proppants and additional chemicals (King, 2012). Water can easily be obtained and pressurized. However, after hydraulic fracturing operations, it is difficult to withdraw the injected water, which might cause a significant decrease in productivity or increase in adverse chemical reactions (Page and Miskimins, 2009; Ribeiro and Sarma, 2013). Thus, it is critically important to accurately estimate fracture propagation as well as fluid flow and proppant migration.

In this study, we numerically investigate fracture propagation and multiphase flow induced by water injection during hydraulic fracturing operations. Note that hydraulic fracture propagation might not be the same as propagation of the water front or proppant (Raterman et al., 2017). Fracturing is governed by geomechanics, whereas water saturation is determined by multiphase flow. The inconsistency between the fracture volume and the injected-water volume implies that we cannot properly estimate the dimension of the fracture by simply assuming the fracture to be fully saturated with the injected water. Thus, for reliable full 3D rigorous modeling, we employ a numerical method that can model tensile failure due to normal and shear stresses, dynamic nonlinear permeability and geomechanical moduli, leak-off in all directions during hydraulic fracturing, and thermo-poro-mechanical effects (Kim and Moridis, 2013). In this study, we find that a significant gap between the water front and the fracture top can occur.

Along with the 3D modeling of vertical fracture propagation and multiphase flow, it is also important to develop and evaluate geophysical methods for monitoring the migration pathways of the injected fluid. Microseismic methods have been widely used in the past decade for estimation of fracture propagation and geometry (Warpinski et al., 2005; Vermylen and Zoback, 2011). In some cases, however, the magnitudes of microearthquakes have been too small to be reliably recorded in practice. In addition, the microseismic inversion for determining the fracture length and width depends strongly on an initial velocity model, and can result in significant ambiguity in hydraulic fracture characterization (Johnson and Shrallow, 2011). To reduce the ambiguity in the microseismic monitoring, we can consider an electromagnetic (EM) geophysical method. When hydraulic fracturing operations force a mixture of fluids and proppant into the formation under high pressure, they generate highly localized changes in porosity and pore fluids. Because EM methods are sensitive to porosity, fluid saturation, and the chemistry of the fluid in pore spaces, they are a promising tool for illuminating migration pathways taken by the injected fluid and proppant, and can complement microseismic methods. In

this study, we investigate the sensitivity of the EM geophysical method to electrical conductivity changes that are directly correlated with hydraulic fracturing operations.

Accordingly, this paper consists of two major parts: coupled flow-geomechanical modeling and EM geophysical modeling. The remainder of this paper is organized as follows: First, we briefly describe a T+M coupled flow-geomechanical modeling algorithm, and then simulate fracture propagation considering coupled non-isothermal flow-geomechanical processes in a tight shale gas reservoir. From this simulation, we obtain changes in the reservoir porosity and permeability, pressure and saturation of gas and water, and fracture openings and displacement over the domain. The resulting reservoir parameters are employed to construct a series of realistic 3D electrical conductivity models using a rock physics model. Subsequently, we evaluate the sensitivity of an EM geophysical method to conductivity changes due to hydraulic fracturing operations. We demonstrate that we can significantly improve the sensitivity of the EM method to the pathways of injection-fluid migration by using electriomagnetically engineered high-conductivity fluids.

2. Hydraulic Fracturing Simulation

2.1. Water injection

Two phase flow within a fracture occurs during water injection during hydraulic fracturing processes. As water flows through the fracture, the water is pressurized and some of the water leaks off into the reservoir formation, as shown in Figure 1. A stimulated zone is shown in the left figure, which consists of a main fracture, several fissures, and partially continuous small fractures, depending on the complexity of the hydraulic fractures (Fisher and Warpinski, 2012). We can model flow and geomechanics of different fractures, using the dual continuum (also called double porosity) approach. Within the hydraulic fracture, while the injected water can leak off to the stimulated zone and/or rock matrix, existing reservoir gas can also flow into the vacuum area near the fracture tip (the right of Figure 1).

Consider a case in which reservoir pressure and temperature are 17.1 MPa and 58.8 ^oC, respectively, selected from a generalized model of Marcellus shale. Viscosities for liquid water and gas phases are $4.79 \times 10^{-4}\ Pa \cdot s$ and $1.78 \times 10^{-5}\ Pa \cdot s$, respectively. Gas density under reservoir conditions, $1.15 \times 10^2\ kg \cdot m^{-3}$, cannot be neglected, compared with the density of water, $9.89 \times 10^2\ kg \cdot m^{-3}$. From the densities and viscosities of water and gas, we can estimate the pattern of water-saturation movement due to buoyancy, constructing the following equation of the fractional flow curve, f_w, after ignoring the gradient of capillary pressure within a

fracture.

$$f_w = \frac{1 - N_g k_{r,g}}{1 + \frac{k_{r,g}}{\mu_g}\frac{k_{r,w}}{\mu_w}}, \quad k_{r,J} = max\left\{0, min\left\{\frac{S_J - S_{r,J}}{1 - S_{r,w}}, 1\right\}\right\} \tag{1}$$

where N_g, $k_{r,J}$, and μ_J are the gravity number, relative permeability and viscosity of phase J, respectively. Subscripts g and w indicate gas and water phases, respectively. S_J and $S_{r,J}$ are, respectively, saturation and residual (irreducible) saturation of phase J. Here we use the modified versions of Stone's relative permeability model.

Figure 2 shows the fractional flow curves with various gravity numbers. From Figure 2, we estimate the movement of water saturation to be piston-like displacement, generating a shock wave. On the other hand, an aperture distribution along the fracture from geomechanics is continuous. Reservoir gas would then be accumulated within the upper area of the fracture, which yields a *dry zone*. We can anticipate that the gas volume within the fracture would become larger as the simulated zone becomes larger, because reservoir gas that fills the simulated zone moves upward due to buoyancy. Another important issue is how much water infiltrates into the reservoir, because leak-off of water into the damaged zone or rock matrix can significantly affect the mobility of gas, reducing relative permeability, when gas is produced.

2.2. Failure condition and permeability

Hydraulic fracturing is based on tensile failure, which creates a fracture and then opens it. We employ a stress-based failure condition for large-scale fracture propagation, rather than a toughness-based condition, using a failure condition Ruiz et al. (2000), written as

$$\sigma'_c \left(= \sqrt{\beta^{-2}({t'_t}^2 + {t'_s}^2) + {t'_n}^2}\right) \leq T_c, \tag{2}$$

where σ'_c is the effective stress for tensile failure, which consists of shear and normal effective stresses. t'_n, t'_t and t'_s are normal and shear effective stresses acting on a fracture plane (Figure 3), and T_c is tensile strength. Using β of Equation 2, we account for the contribution of shear effective stress to tensile failure.

When implementing the tensile failure, we implicitly employ a node-splitting scheme, as shown in Figure 3 (left). Then, considering vertical fracture propagation, we can simplify the node-splitting scheme into a method that updates outer boundary conditions (i.e., from the Dirichlet condition to the Neumann condition, as shown in Figure 3 (right)), not introducing an internal boundary (this scheme was previously used in Ji et al. (2009)). We then can reduce computational resources and code management effort.

For the modeling of the fracture permeability corresponding to tensile failure, we use the modified cubic law (e.g., Snow (1965) and Rutqvist and Stephansson (2003)), written as

$$Q_w = a_c \frac{\omega_f^3}{12\mu_w} H \left(\mathbf{Grad}\, p_w - \rho_w \mathbf{g} \right), \tag{3}$$

where ω_f is the aperture, also called fracture opening. Q_w is flow rate of water, H is the fracture plate width, and g is the gravity vector. a_c is the correction factor that reflects the fracture roughness. We use a minimum fracture permeability, still much higher than the permeability of intact rock, when the fracture is re-closed.

2.3. Coupled flow and geomechanics

We employ quasi-static mechanics from momentum balance, when solving geological deformation and failure. Governing equations of fluid and heat flow are derived from conservation laws of fluid mass and energy. In hydraulic fracturing operations, flow and geomechanics are tightly coupled, because permeability is a strong function of material failure and deformation of a fracture, as described in Equation 3. The high deformability of the fracture also affects coupling in pore volume, which cannot be neglected; this coupling can be modeled by poromechanics (Coussy, 2004). Specifically, according to Berryman (2002) and Kim et al. (2012), the porosity coupling using a multiple continuum approach, which can represent a fracture-rock matrix system (or a system of the main fracture and small local fractures), can be written as

$$\delta\Phi_l = \left(\frac{\alpha_l^2}{K_{dr}} + \frac{\alpha_l - \Phi_l}{K_s} \right) \delta p_l + 3\alpha_{T,l}\alpha_l \delta T_l - \frac{b_l}{\eta_l}\sigma_v, \quad b_l = -\frac{\alpha_l \eta_l}{K_l}, \tag{4}$$

where Φ_l is the Lagrange porosity, defined as the ratio of the pore volume in the deformed configuration to the bulk volume in the reference (initial) configuration. The subscription l indicates subelements in a gridblock. T is temperature. K_l, K_s, η_l, $\alpha_{T,l}$, α_l are the drained bulk modulus, intrinsic solid grain modulus, volume fraction, thermal dilation coefficient, and Biot's coefficient for subelement l within a gridblock, respectively. σ_v is total mean (volumetric) stress at the gridblock.

In numerical modeling, we employ the finite volume method for flow, in which flow variables take piecewise-constant interpolation. For geomechanics, we use the finite element method, taking linear interpolation of displacement. In time discretization, we employ the backward Euler method. (These discretizations for flow and geomechanics are widely used in reservoir simulation and computational geomechanics communities, respectively.)

We employ a sequential method to solve coupled flow and geomechanics problems. Specifically, we use the

fixed-stress sequential method in solving two-way coupling in pore-volume, written as (Kim et al., 2012)

$$\Phi^{n+1} - \Phi^n = \underbrace{\left(\frac{\alpha_l^2}{K_{dr}} + \frac{\alpha_l - \Phi^n}{K_s}\right)}_{\Phi^n c_p} \sum_J S_J^{n+1}\left(p_l^{n+1} - p_l^n\right) + \underbrace{3\alpha_{T,l}\alpha_l}_{\Phi^n c_T}(T_l^{n+1} - T_l^n) - \underbrace{\frac{b_l}{\eta_l}\left(\sigma_v^n - \sigma_v^{n-1}\right)}_{\Delta\Phi}, \quad (5)$$

where the superscript n is the time level in time discretization. c_p and c_T correspond to the pore compressibility and thermal expansivity used in reservoir simulation, respectively. $\Delta\Phi$ is called porosity correction, calculated from the previous geomechanics solutions, which can capture poromechanical effects such as the Mandel-Cryer effect.

Permeability is calculated based on geomechanics solution, e.g., failure status and aperture of the fracture at the previous time step. Because the permeability is a strong function of geomechanical failure, for further accuracy, we take a small time-step size that ensures no fracturing between two fracturing events.

From the given numerical schemes, we can make use of existing flow and geomechanics codes by constructing an interface between them. In this study, we couple TOUGH+RealGasH2O, a flow simulator, to ROCMECH, a geomechanics simulator, (shortly T+M). T+M carried out several verification tests for thermo-poro-mechanics (e.g., the Terzaghi, Mandel, and McNamee-Gibson problems), the opening of static fractures, and fracture propagations for viscosity and toughness-dominated systems, matching the analytical solutions (e.g., Kim and Moridis (2013)).

2.4. Simulation domain

Assuming a 3D simulation domain, as shown in Figure 4, we discretize the domain for geomechanics with 50, 5, and 50 gridblocks in x, y, and z directions, respectively. The direction of the minimum compressive principal total stress is perpendicular to the x-z plane. Gridblock sizes in the x and z directions are uniform, i.e., $\Delta x = \Delta z = 3\ m$. The sizes of the gridblocks in the y direction are non-uniform, i.e., 0.1 m, 0.5 m, 3.0 m, 10.0 m, and 20.0 m. We take Young's modulus (E) of 12 GPa and Poisson's ratio (ν) of 0.3, respectively. The tensile strength of shale for the reference case is $T_c = 10\ MPa$. We assume $\beta = 1.0$ for contribution of effective shear stress to tensile failure.

For flow, we take the same discretized domain of geomechanics, having 50, 6, and 50 gridblocks in x, y, and z directions, respectively, with an additional layer in the y direction. The additional layer, the thickness of which is 1.0 m, represents half of the width of the stimulated reservoir zone shown in Figure 1. We assume water to be injected at (x=75 m , z=-1440 m), which is an initial fractured node. We take $8.645 \times 10^{-18}\ m^2$ for the intrinsic permeability of the rock matrix, where 1 darcy is $9.87 \times 10^{-13}\ m^2$. For relative permeability, we

use $S_{r,w} = 0.08$ and $S_{r,g} = 0.01$. In addition, $a_c = 0.14$ is taken for the modified cubic law. Biot's coefficient (α) is 1.0, and the thermal dilation coefficient (α_T) is $4.5 \times 10^{-6}\ ^oC$. We apply the dual continuum approach only to the stimulated zone (i.e., the additional layer), consisting of the main fracture and the damaged zone, while the single continuum approach is employed for the other area.

The permeability of the main fracture, k_f^p, is calculated from Equation 3; the permeability of the damaged zone, k_m^p, is calculated from $k_m^p = \chi^m k_f^p$. χ^m is a parameter that characterizes degrees of small fractures near the main fracture, which affects leak-off of water. In this study, χ^m is simply assigned 10^{-3}, while χ^m could be determined more systematically, for example, on the basis of upscaling the modeling of small fracturing near the main fracture, or inverse calculation from the leak-off data. The lower limit of k_f^p is 60 mD in this study. For Equation 5, we assume $K_l = 500\ MPa$ for both continua (i.e., hydraulic fracture and stimulated zone). We take $\eta_f = 0.01$ and $\eta_f = 0.99$.

For the initial conditions, reservoir pressure is initially 17.10 MPa at the depth of 1350 m (z=-1350 m), with a 12.44 kPa/m gradient. Initial temperature is 58.75 ^oC at z=-1350 m, with a 0.025 $^oC/m$ gradient. Based on estimation of the generic total stress distribution (Zang and Stephansson, 2010), the initial total principal stresses are -36.40 MPa, -23.30 MPa, and -29.12 MPa at z=-1350 m in x, y, and z directions, respectively, where tensile stress is positive. The corresponding stress gradients are -27.0 kPa/m, -17.59 kPa/m, and -21.57 kPa/m, respectively. The injection rate is 40 kg/s at the injection point with no-flow boundary conditions for flow. For geomechanics, there are no-horizontal-displacement boundary conditions for the sides, except for the fractured nodes, with no displacement boundary at the bottom. We have bulk density of 2200 $kg \cdot m^{-3}$, considering gravity.

For capillarity, we use the van Genuchten capillary pressure model (van Genuchten, 1980), written as

$$P_c = \Pi_c \left(\left(\frac{S_w - S_{r,w}}{1 - S_{r,g} - S_{r,w}} \right)^{-1/\lambda_p} - 1 \right)^{1-\lambda_p}, \tag{6}$$

where P_c, λ_p and Π_c are the capillary pressure, exponent that characterizes the capillary pressure curve, and capillary modulus, respectively. We take $\lambda_p = 0.45$ and $\Pi_c = 20\ kPa$ in Equation 6. $S_{r,w} = 0.05$ and $S_{r,g} = 0.0$ are used for capillarity, slightly smaller than those used in the relative permeability model, in order to prevent unphysical behavior (Moridis et al., 2008).

3. Numerical Results of fracture propagation

Figure 5 shows fracture propagation and fracture opening for the main fracture at different times. Because of a point source of the water injection, the fracture propagates in an elliptic shape, as shown in the left figure. As shown in the right of Figure 5, the aperture of the fracture is continuous when the fracture is open. The fracture propagation is stable, which implies that the propagation depends on the injection time and that it can be controlled by the injection rate and time.

Figure 6 shows flow and geomechanical responses at different monitoring points. Fracturing occurs more at early times than at late times. Due to discontinuity of the fracturing events in time, we identify pressure fluctuation under the constant rate of water injection, observing that pressure drops every time when failure occurs. The pressure fluctuation becomes severer at early times than at late times, because the fracture volume is small at early times. Pressure responses of incompressible fluid are more sensitive to smaller fractured areas. Then, the fluctuation decreases as the fracture length grows and the fractured area becomes large. This pressure oscillation can also be found in Tzchichholz and Herrmann (1995). Along with the pressure fluctuation, the fracture aperture exhibits the same behavior as pressure. For displacement, we observe the uplift at the top of the simulation domain, owing to expansion of the domain induced by fluid injection.

In Figure 7, we find the existence of reservoir gas within the fracture. In particular, we identify a large amount of gas within the fracture at late times. As the fracture grows, reservoir gas initially captured in the stimulated zone moves upward due to buoyancy, occcupying the upper part of the fracture, while the injected water fills the lower part of the fracture because of the higher density. From Figure 8, we also find that, at early times, the water front (water saturation) is almost identical to the fracture tip, indicating that the fracture is mostly filled with injected water. However, at late times, the water front's advance is retarded compared to the fracture propagation, yielding a significant gap between the water front and the fracture top, filled with reservoir gas. Fracture propagation is not the same as water-front propagation, because fracturing is determined by geomechanics while water saturation is by multiphase flow. We thus cannot assume the fracture to be fully saturated with the injected water when estimating the dimensions of the fracture.

In Figure 9, we find considerable leak-off of water to the reservoir. Gas saturations within the damaged zone and intact reservoir nearest to the stimulated zone are significantly low, indicating that a considerable amount of water has infiltrated into the reservoir.

4. Electromagnetic Monitoring of Fluid Migration Pathways

EM geophysical responses to an Earth model are governed by solving Maxwell's equations in the frequency domain. We consider the finite-element formulation for solving the electric-field diffusion equation numerically (Um et al., 2017c). Then, the magnetic fields are interpolated from the electric fields using Faraday's law. The matrix system is unstructured, sparse, complex, and symmetric, and it is solved using a parallel direct solver, MUMPS (MUltifrontal Massively Parallel Sparse direct Solver) (Amestoy et al., 2006), in this study.

4.1. Electrical conductivity models

Once a set of reservoir parameters (e.g., porosity Φ, water saturation S_w, and electrical conductivity of water, k_w^σ) are determined from coupled flow-geomechanical simulation, the bulk electrical conductivity k^σ of a shaly reservoir can be estimated by Waxman-Smits equation (Waxman and Smits, 1968; Kwon and Snieder, 2011):

$$k^\sigma = \Phi^{m_e} S_w^{n_e} \left(k_w^\sigma + 4.78 \times 10^{-8} \left[1 - 0.6exp(-\frac{k_w^\sigma}{0.0013}) \right] Q_v S_w^{-1} \right), \quad Q_v = \rho_g \frac{1-\Phi}{\Phi} C_e, \tag{7}$$

where ρ_g is the grain density. C_e is the cation exchange capacity. The exponents, m_e and n_e, are the exponents that characterize the electrical conductivity. In this study, the rock physics parameters of Equation 7 are empirically chosen; m_e and n_e, are set to 2; $\rho_g = 2,370\ kg \cdot m^{-3}$; $C_e = 38,000\ Coulomb/kg$; $k_w^\sigma = 3.33\ S/m$. Thus, Equation 7 can transforms the reservoir parameters to electrical conductivity values.

Hydraulic fracturing operations force fluids into the formation under high pressure, producing highly localized changes in porosity and pore fluids. Because EM geophysical methods are sensitive to the porosity, fluid saturation, and chemistry of the fluid in the pore space, they are a promising tool for illuminating injected-fluid migration pathways.

One primary goal of our EM modeling analysis is to examine the capabilities of an EM geophysical method for sensing bulk conductivity changes that are directly related to migration pathways of injected fluids. For successful EM detection of fluid movement, it is important to ensure a sufficient contrast in electrical conductivity between the intact and stimulated zones. This sufficient contrast can be realized by injecting the brine (3.3 20 S/m). When a larger contrast is required to detect fractures at deeper depths or away from EM sensors in monitoring wells, we can also consider electromagnetically engineered injection fluids that have high magnetic permeability and/or electrical conductivity values. The engineered fluids avoid utilizing chemical additives because they can change fluid chemistry and negatively influence fracturing fluid performance. Instead, it is

considered practical and effective to utilize a low-cost and low-density suspension with metallic-like conductivity such as colloidal graphite (Tang et al., 1999). For detailed information about the applications of such fluids, the reader is referred to Borglin et al. (2000) and Oldenburg et al. (2000). Recently, Salis (2012) also shows that a mixture of water and electrically-coated proppants can ensure large constrasts in conductivity between the intact and stimulated zones. In short, it is technically feasible to employ electromagnetically engineered fluids in hydraulic fracturing operations.

Based on the Waxman-Smits equation, we can transform reservoir parameters to electrical conductivity models. Figure 10 shows cross-sectional views of reservoir parameters (the first column for reservoir porosity, the second column for fluid saturation, and the third column for electrical conductivity after hydraulic fracturing starts, along with a high-conductivity fluid (10,000 S/m). In Figure 10, porosity and saturation are volume-averaged within the stimulated zone. For comparison purposes, we also generate the electrical conductivity models (the fourth column) when the brine (3.33 S/m) is injected. As the hydraulic fracturing operation continues, perturbations in porosity and saturation gradually increase in all directions (e.g., leak-off of water).

Note that because fracture propagation is not the same as injected fluid movement, the anomalous conductivity distribution gradually deviates over time from the anomalous porosity distribution, and increasingly resembles the anomalous saturation distribution. Accordingly, EM responses to the given conductivity models will be more directly correlated with the migration pathways of the injected fluids, but might be marginally sensitive to unsaturated fractures. Therefore, when EM geophysical methods are used to characterize hydraulically induced fractures, one should be aware of the possibility that the unsaturated fractures may not be imaged. In contrast, as mentioned earlier, microseismic methods are based on seismic events associated with fracturing, but are insensitive to saturation changes at late times. Therefore, we can expect that the joint analysis of microseismic and EM data would significantly reduce the ambiguity involved in characterizing hydraulically induced fractures. Also note that the use of high-conductivity fluid does not change the overall geometry of anomalous conductivity distribution (compare the third column of Figure 10 with the fourth column), but significantly increases the conductivity contrast over time. Thus, as will be demonstrated in the next section, its use makes EM geophysical methods more suitable for monitoring migration pathways of the injected fluids.

5. Crosswell EM methods

As a possible option for monitoring the migration pathways of injected fluids, we employ an EM geophysical method. There are different types of EM methods for the purpose: surface, borehole-to-surface and crosswell EM methods. The surface-based EM method for imaging fractures (e.g. Um et al. (2017b)) has both sources and receivers on the surface and does not require expensive monitoring wells. Thus, the method has relatively low operation costs compared with the crosswell method. However, in order to detect fractures in deep depth, the method must employ low frequency sources, resulting in low resolution. In contrast, the crosswell method allows sources and receivers to be placed directly in deep depth and can be operated at higher source frequencies for higher resolutions. We can also consider a hybrid version of the two methods where sources are placed inside a single monitoring well and receivers are placed on the surface (Um et al., 2017a). In this study, we choose the crosswell EM method over the surface-based EM method since the primary goal of our numerical modeling is to examine the feasibility of the EM methods for monitoring fractures rather than to evaluate the cost effectivenss of the EM methods.

Crosswell EM methods (Figure 11) interrogate electrical conductivity structures between wells and can yield detailed cross-sectional images. These EM methods typically employ solenoids as a transmitter (a wire coil carrying alternating currents). The emitted magnetic source fields are called primary magnetic fields (B_o) and induce currents in nearby formations. In turn, the induced currents generate secondary magnetic fields. The primary and secondary magnetic fields are measured in the other well with magnetic receivers. The source is excited at different positions in one well and the receiver records the magnetic fields in the other well. Then, the receiver is moved to a next position. We repeat the same process at the different receiver position. After the crosswell EM data are collected, the conductivity structures between the wells are determined through inverse modeling. (For details of the crosswell EM methods and their applications, the reader is referred to Alumbaugh and Morrison (1995), Wilt et al. (1995), Zeng et al. (2000), and Gao et al. (2008)) To successfully sense and monitor injection-fluid migration pathways, conductivity changes caused by migration should produce measurable perturbation in the magnetic fields.

The vertical crosswell EM configuration would work well for sensing the height and width of fractures between wells; the horizontal crosswell EM configuration would be sensitive to the thickness of the fractures. For both crosswell EM configurations, well spacing is set to 100 m. The source frequency is set to 3,000 Hz.

To allow for the high frequency source in a well environment, it is required that part of the casing in which the sources and receivers are placed is composed of nonmetallic materials (e.g., fiberglass). It is also assumed that magnetic receivers can detect a 1% difference in the magnetic field amplitude (i.e. 99% repeatability), and the receiver noise level is 10^{-10} (Ampere/m).

The proposed crosswell EM configurations were simulated using the 3D FE electromagnetic simulator over the electrical conductivity models shown in Figure 10 (Um et al., 2017c). Vertical crosswell EM responses to the conductivity models with the high-conductivity fluid and the brine are shown at selected source positions in Figures 12 and 13, respectively. Horizontal crosswell EM responses to the conductivity models using high-conductivity fluid and the brine are shown in Figures 14 and 15, respectively. For simplicity, the total magnetic fields and their relative difference with respect to the magnetic fields of 0.02 S/m half-space (i.e., the background conductivity before the injection) are plotted. First, note that all magnetic fields (the left column of Figures 12 through 15) are above the noise level prescribed above. As the fracture grows larger, both horizontal and vertical crosswell measurements start to sense the fracture. When the brine is injected, the perturbation in the magnetic field is marginal (Figures 13 and 15). However, this does not imply that the brine is an ineffective tracer when the crosswell EM method is employed to map saturated fractures. In fact, the brine movements have been successfully detected in many enhanced oil recovery operations. However, in this particular case, the brine injection produces few changes in conductivity (the fourth column of Figure 10), due to the limited increase in porosity (from 0.049 to 0.059) during hydraulic fracturing, resulting in marginal perturbation of the magnetic field. In contrast, Figures 12 and 14 show that the use of high-conductivity fluid significantly improves (to about an order of magnitude) the sensitivity of crosswell EM measurements to conductivity changes due to hydraulic fracturing operations. We conclude that along with an electromagnetically engineered fluid, the crosswell EM method can serve as an effective mapping tool for conductivity changes directly related to the migration pathways of the injected fluid.

6. Conclusions

We have investigated geomechanical and flow responses induced by water injection during hydraulic fracturing operations. From the numerical results, we have found that fracture propagation was not the same as propagation of the water front. The gap between the water front and the fracture top was more dominant at later times, after a large amount of water was injected. The inconsistency between the fracture volume and the

volume of injected water could lead to underestimating the fracture propagation, if we were to make the simple assumption that the fracture is fully saturated with the injected water. We have identified fluctuation in pressure and displacement under constant water injection. As the fracture dimension became larger, the fluctuation decreased. All the complex physical processes in this study are fundamentally based on tight coupling between flow and geomechanics, exhibiting different time scales between them.

Owing to the rigorous 3D modeling capabilities of a recently developed coupled flow-geomechanical simulator, T+M, we have been able to generate a series of physically realistic electrical conductivity models that reveals transient changes in conductivity within shaly reservoirs during hydraulic fracturing operations. Because movement of the injected fluid is separated from the fracture propagation at late times, conductivity models are more closely related with the migration pathways of the injected water rather than unsaturated fractures. The 3D finite element method for Maxwell's equations was used in this study to simulate crosswell EM methods over a series of conductivity models. Our modeling analysis of this study suggests that the crosswell EM method can serve as an effective mapping tool for conductivity changes along the migration pathways of the injected fluids. Since our sensitivity analysis demonstrates sufficient perturbation in the magnetic fields during hydraulic fracturing, we expect that 3D inverse modeling of the crosswell EM measurements will be able to determine spatial distribution of electrical conductivity around the wells, and make it possible to delineate fluid-migration pathways and fracture geometry. The resulting conductivity images will also provide a clearer understanding of the fractured reservoir. We will further conduct sensitivity analyses with different types of electromagnetically engineered fluids and proppants, optimal geophysical survey designs (both borehole-based and surface-based) for typical hydraulic fracturing scenarios and subsequent geophysical imaging experiments in our future research.

Acknowledgements

This study was supported by the US Environmental Protection Agency, Office of Water, under an Interagency Agreement with the U.S. Department of Energy at the Lawrence Berkeley National Laboratory through Contract No. DE-AC02-05CH11231, and by RPSEA (Contract No. 08122-45) through the Ultra-Deepwater and Unconventional Natural Gas and Other Petroleum Resources Research and Development Program as authorized by the US Energy Policy Act (EPAct) of 2005. The research described in this article has been funded wholly (or in part) by the U.S. Environmental Protection Agency through Interagency Agreement (DW-89-92235901-C) to the Lawrence Berkeley National Laboratory. The views expressed in this article are those of

the author(s) and do not necessarily reflect the views or policies of the EPA.

References

Adachi, J., Siebrits, E., Peirce, A., Desroches, J., 2007. Computer simulation of hydraulic fractures. Int. J. Rock Mecha. Min. Sci. 44, 739–757.

Alumbaugh, D., Morrison, H., 1995. Monitoring subsurface changes over time with cross well electromagnetic tomography. Geophys. Prospect. 43, 873–902.

Amestoy, P.R., Guermouche, A., L'Excellent, J.Y., Pralet, S., 2006. Hybrid scheduling for the parallel solution of linear systems. Parallel Comput. 32, 136–156.

Arthur, J.D., Layne, B.B.M., 2008. Hydraulic fracturing considerations for natural gas wells of the marcellus shale, in: Ground Water Protection Council 2008 Annual Forum, Cincinati, Ohio.

Berryman, J.G., 2002. Extension of poroelastic analysis to double-porosity materials: New technique in micro-geomechanics. Journal of Engineering Mechanics-ASCE 128, 840 – 847.

Borglin, S., Moridis, G., Oldenburg, C., 2000. Experimental studies of the flow of ferrofluids in porous media. Transport Porous Med. 41, 61–80.

Cipolla, C., Lolon, E., Rubin, B., 2010. Reservoir modeling in shale-gas reservoirs. SPE Reserv. Eval. Eng. , 638–653.

Coussy, O., 2004. Poromechanics. John Wiley and Sons, Chichester, England.

Dean, R.H., Schmidt, J.H., 2009. Hydraulic fracture predictions with a fully coupled geomechanical reservoir simulation. SPEJ 14, 707–714.

Fisher, K., Warpinski, N., 2012. Hydraulic fracture-height growth: real data. SPE Prod. Oper. 27, 8–19.

Fjaer, E., Holt, R.M., Horsrud, P., Raaen, A.M., Risnes, R., 2008. Petroleum Related Rock Mechanics. Elsevier B.V., Amsterdam, The Netherlands. second edition.

Gao, G., Alumbaugh, D., Zhang, P., Zhang, H., Levesque, C., Rosthal, R., Liu, J., Abubakar, A., Habashy, T., 2008. Practical implications of nonlinear inversion for cross-well electromagnetic data collected in cased-wells, in: SEG Annual Meeting Abstract, Las Vegas, Nevada. pp. 299–303.

van Genuchten, 1980. A closed-form equation for predicting the hydraulic conductivity of unsaturated soils. Soil Sci Soc Am J. , 892–898.

Ji, L., Settari, A., Sullivan, R.B., 2009. A novel hydraulic fracturing model fully coupled with geomechanics and reservoir simulation. SPEJ 14, 423–430.

Johnson, R., Shrallow, J., 2011. Ambiguity in microseismic monitoring, in: SEG Annual Meeting Abstract, San Antonio, Texas.

Kargbo, D.M., Wilhelm, R.G., Campbell, D.J., 2010. Natural gas plays in the marcellus shale: Challenges and potential opportunities. Environ. Sci. Technol. 44, 5679–5684.

Kim, J., Moridis, G.J., 2013. Development of the t+m coupled flow-geomechanical simulator to describe fracture propagation and coupled flow-thermal-geomechanical processes in tight/shale gas systems. Comput. Geosci. 60, 184–198.

Kim, J., Sonnenthal, E., Rutqvist, J., 2012. Formulation and sequential numerical algorithms of coupled fluid/heat flow and geomechanics for multiple porosity materials. Int. J. Numer. Meth. Engrg. 92, 425–456.

King, G.E., 2012. Hydraulic fracturing 101: What every representative, environmentalist, regulator, reporter, investor, university researcher, neighbor and engineer should know about estimating frac risk and improving frac performance in unconventional gas and oil wells., in: Hydraulic Fracturing Technology Conference, Woodland, TX.

Kwon, M., Snieder, R., 2011. Uncertainty analysis for the integration of seismic and controlled source electromagnetic data. Geophys. Prospect. 59, 609–626.

Moridis, G.J., Kowalsky, M.B., Pruess, K., 2008. Tough+hydrate v1.0 user's manual: A code for the simulation of system behavior in hydrate-bearing geologic media, in: Report LBNL-00149E, Lawrence Berkeley National Laboratory, Berkeley, CA.

Nordren, R.P., 1972. Propagation of a vertical hydraulic fracture. SPEJ 12, 306–314. SPE 7834.

Oldenburg, C., Borglin, S., Moridis, G.J., 2000. Numerical simulation of ferrofluid flow for subsurface environmental applications. Transport Porous Med. 38, 319–344.

Osborn, S.G., Vengosh, A., Warner, N.R., Jackson, R.B., 2011. Methane contamination of drinking water accompanying gas-well drilling and hydraulic fracturing. Proceedings of the National Academy of Sciences 108, 8172–8176.

Page, J.C., Miskimins, J.L., 2009. A comparison of hydraulic and propellant fracture propagation in a shale gas reservoir. J. Can. Petrol. Technol. 48, 26–30.

Perkins, T.K., Kern, L.R., 1961. Widths of hydraulic fractures. J. Pet. Technol. 13, 937–949. SPE 89.

Raterman, K.T., Farrell, H.E., Mora, O.S., Janssen, A.L., Gomez, G.A., Busetti, S., McEwen, J., Davidson, M.D., Friehauf, K., Rutherford, J., Reid, R., Jin, G., Roy, B., Warren, M., 2017. Sampling a stimulated rock volume: An eagle ford example, in: Unconventional Resources Technology Conference, Austin, TX. URTeC-2670034.

Ribeiro, L.H., Sarma, M.M., 2013. Fluid selection for energized fracture treatments, in: SPE Hydraulic Fracturing Technology Conference, The woodland, TX.

Ruiz, G., Ortiz, M., Pandolfi, A., 2000. Three-dimensional finite-element simulation of the dynamic brazilian tests on concrete cylinders. Int. J. Numer. Meth. Engrg. 48, 963–994.

Rutqvist, J., Rinaldi, A., Cappa, F., Moridis, G., 2013. Modeling of fault reactivation and induced seismicity during hydraulic fracturing of shale-gas reservoirs. J. Pet. Sci. Eng. 107, 31–44.

Rutqvist, J., Stephansson, O., 2003. The role of hydromechanical coupling in fractured rock engineering. Hydrogeol. J. 11, 7–40.

Salis, N., 2012. Study on the feasibility of using electromagnetic methods for fracture diagnostics. MS. thesis. University of Texas at Austin.

Snow, D., 1965. A parallel plate model of fractured permeable media. PhD thesis. University of California at Berkeley.

Tang, B., Geng, Y., Lam, J., Li, B., Jing, X., Wang, X., Wang, F., Pakhomov, A.B., Zhang, X.X., 1999. Processible nanostructured materials with electrical conductivity and magnetic susceptibility: Preparation and properties of maghemite/polyaniline nanocomposite film. Chem. Mater. 11, 1581–1589.

Tzchichholz, F., Herrmann, H.J., 1995. Simulations of pressure fluctuations and acoustic emission in hydraulic fracturing. Phys. Rev. E 51, 1961–1970.

Um, E.S., Kim, J., Fu, H., 2017a. New advances in 3d borehole-to-surface electromagnetic modeling and imaging in the presence of steel-cased wells. Geophys. J. Int. Under review.

Um, E.S., Kim, J., Kim, S., Commer, M., 2017b. A feasibility study on a casing-top electric source method for detecting and imaging hydraulically active fractured zones: 3d finite element modeling approach. Geophys. J. Int. In minor revision.

Um, E.S., Kim, S., Fu, H., 2017c. A tetrahedral mesh generation approach for 3d marine controlled-source electromagnetic modeling. Comput. Geosci. 100, 1–9.

Vermylen, J.P., Zoback, M., 2011. Hydraulic fracturing, microseismic magnitudes, and stress evolution in the barnett shale, texas, usa, in: SPE Hydraulic Fracturing Technology Conference, The woodland, TX. Spe 140507.

Warpinski, N.R., Kramm, R.C., Heinze, J.R., Waltman, C.K., 2005. Comparison of single- and dual-array microseismic mapping techniques in the barnett shale, in: SPE Annual Technical Conference and Exhibition, Dallas, TX. SPE95568.

Waxman, M.H., Smits, L.J.M., 1968. Electrical conductivities in oil-bearing shaly sands. SPEJ 8, 107–122.

Wilt, M., Alumbaugh, D., Morrison, H., Becker, A., Lee, K., Deszcz-Pan, M., 1995. Crosshole electromagnetic tomography: System design considerations and field results. Geophysics 60, 871–885.

Zang, A., Stephansson, O., 2010. Stress field of the Earth's crust. Springer Science+Business Media B.V.

Zeng, W., Zhao, W., Wilt, M., 2000. Three successful large-scale field tests of crosshole electromagnetic tomography technology, in: SPE Annual Technical Conference and Exhibition, Dallas, TX. SPE 63143.

Zoback, M., Kitasei, S., Copithorne, B., 2010. Addressing the environmental risks from shale gas development. Worldwatch Institute Briefing Paper 1 (Worldwatch Inst., Washington D.C) .

Zoback, M.D., 2007. Reservoir Geomechanics. Cambridge University Press, Cambridge, UK.

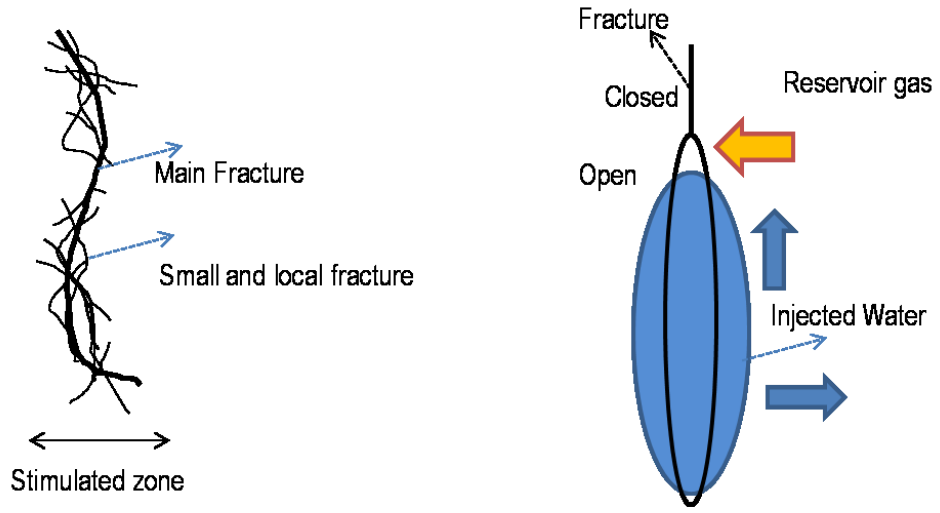

Figure 1: Schematics of complex fractures and fluid movement around the fractures. Left: Hydraulic fractures create different types of the stimulated zone shown. Right: Multiphase flow depends on viscous force, buoyancy, poromechanical effects, and fracture volume.

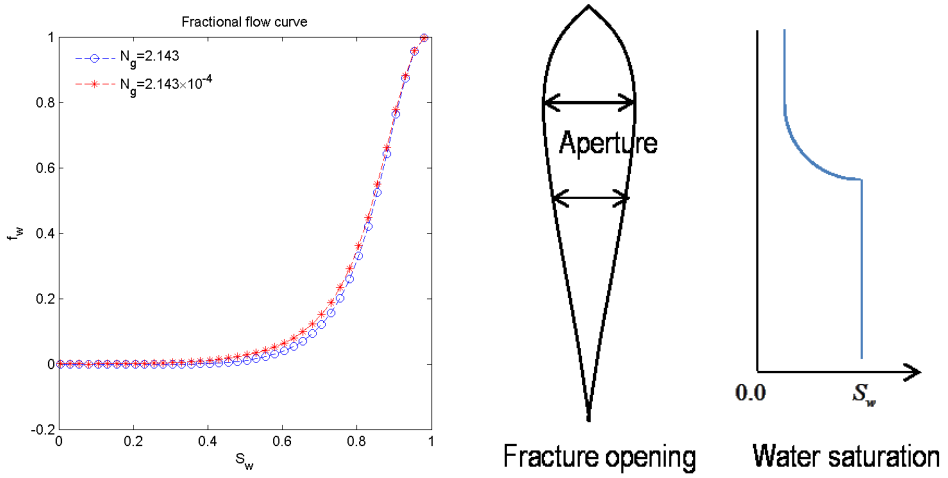

Figure 2: Left: Fractional flow curves at different gravity numbers. Right: Schematics of the fracture opening and water saturation distribution.

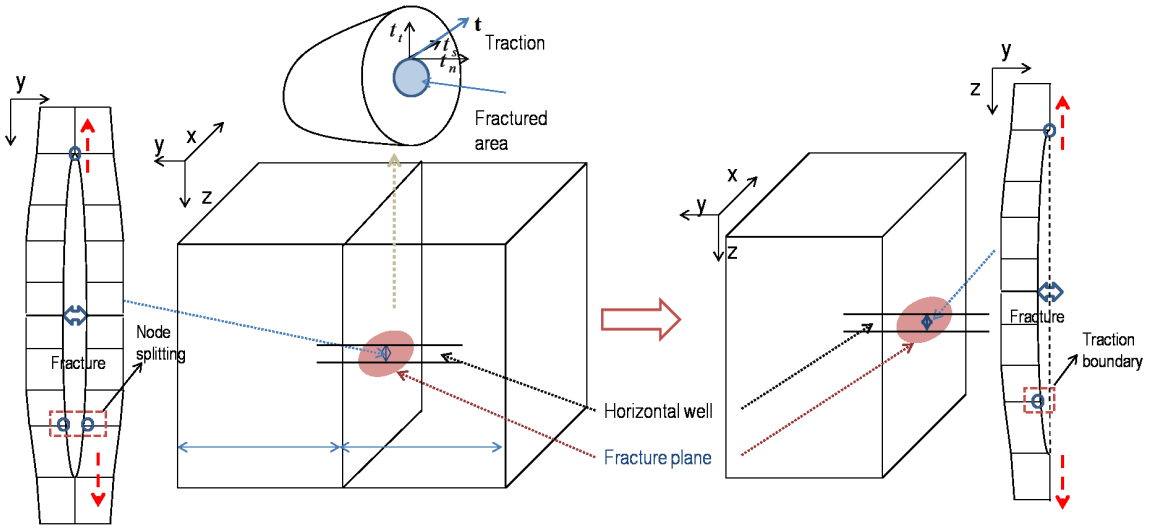

Figure 3: Schematics of tensile failure in 3D. Left: Planar fracture propagation along the vertical direction. Right: Modeling of vertical fracture propagation using no horizontal displacement condition at the plane that contains the vertical fracture (Kim and Moridis, 2013).

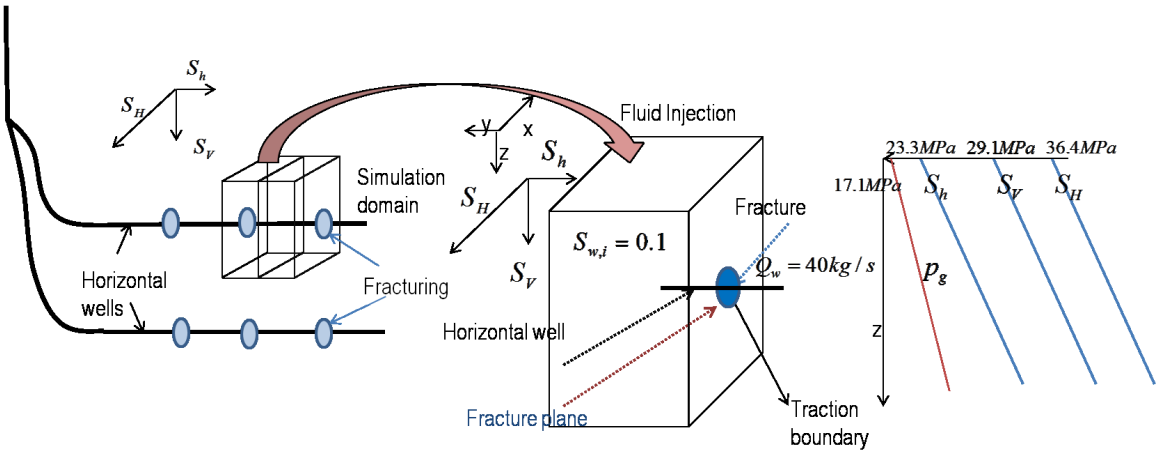

Figure 4: Left: A scenario of simultaneous hydraulic fracturing. Center: The numerical domain of hydraulic fracturing simulation in 3D. Right: Initial distributions of fluid pressure and total principal stresses. We assume a simultaneous fracturing operation, where the horizontal wells are aligned with the direction of the minimum compressive principal total stress, S_h.

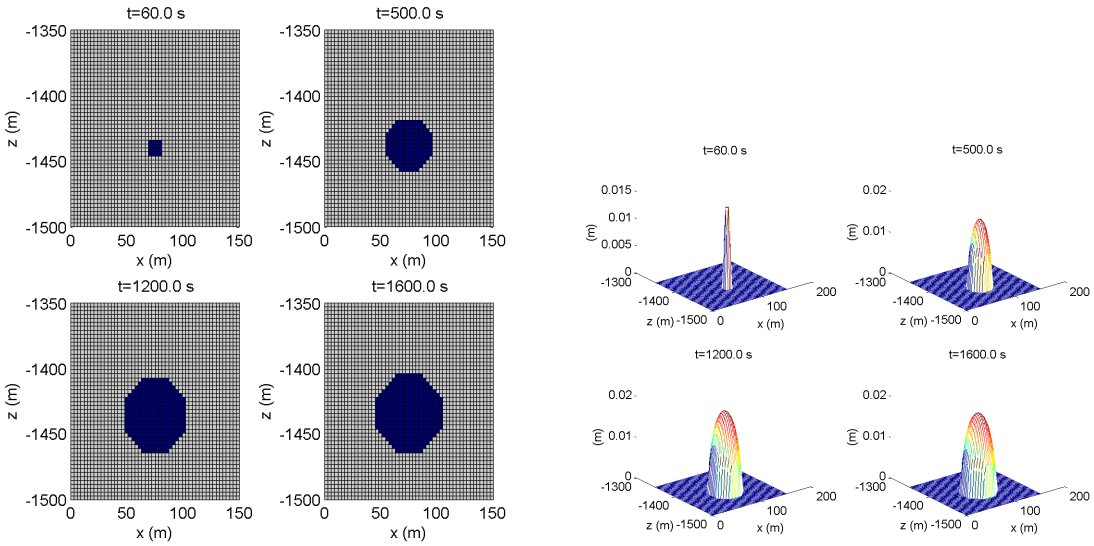

Figure 5: Left: Growth of the vertical fracture induced by water injection. Right: The corresponding fracture opening. The fracture propagation depends on the injection time.

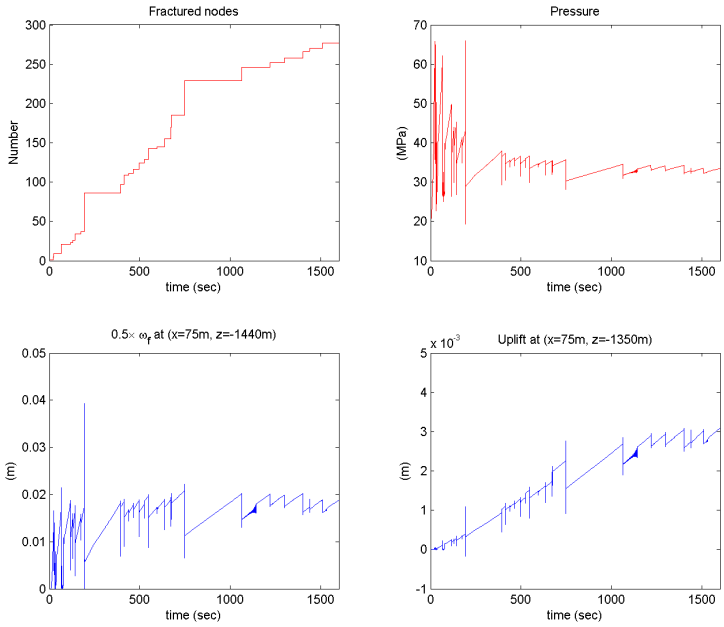

Figure 6: Evolution of geomechanics and flow variables: (a) number of the fractured nodes, (b) pressure at the injection point, (c) aperture of the fracture at the injection point, (d) displacement at (x=75m, z=-1350m). Fracturing events are discontinuous, which results in fluctuation of the pressure and aperture. The oscillation becomes more dominant at early times due to small volume of the fracture.

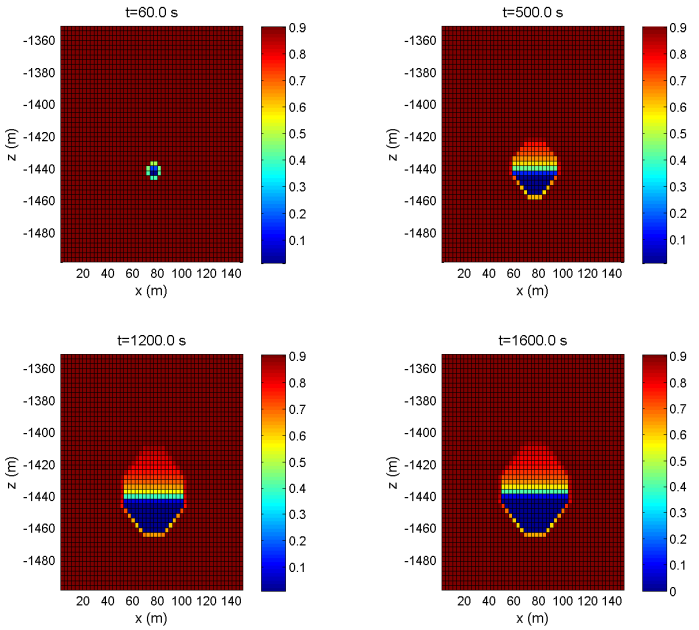

Figure 7: Gas saturation at different times. The color-bar indicates gas saturation. Gas is accumulated at the upper part of the fracture, while water fills the lower part.

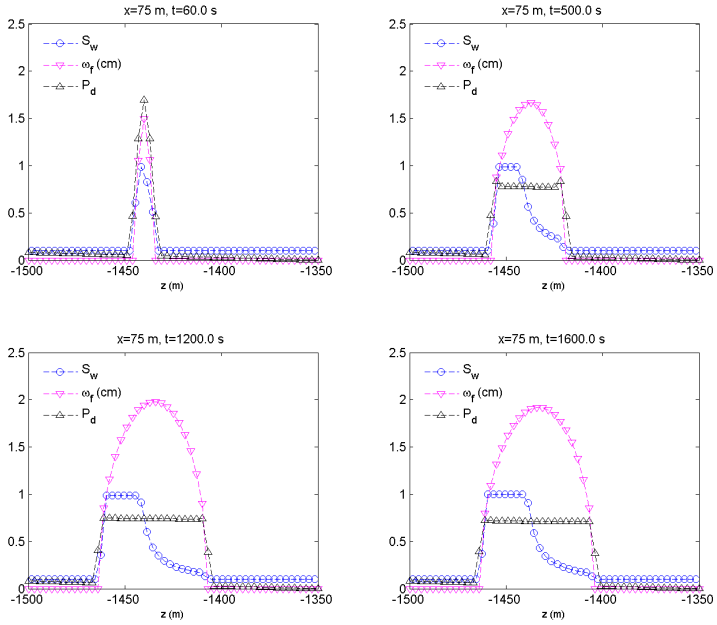

Figure 8: Distributions of water saturation, aperture, dimensionless pressure (p_d) at x=75m. $p_d = \frac{p-p_L}{p_U-p_L}$, where p_U=40MPa and p_L=17.1MPa. The aperture is continuous along the fracture, while gas saturation is somewhat discontinuous. At early times, water fills almost all parts of the fracture, whereas gas takes up a considerable volume within the fracture at late times.

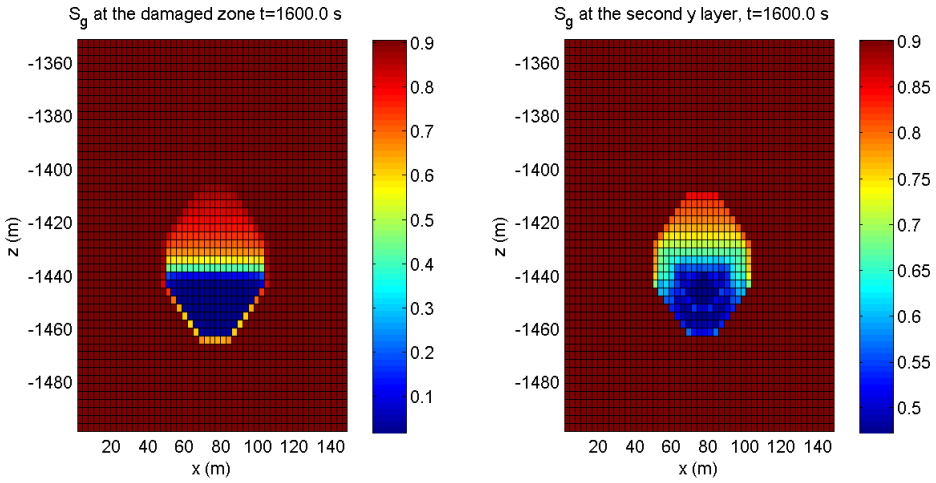

Figure 9: Distribution of gas saturations at the damaged zone (left figure) and the rock matrix (right figure). The large amount of water infiltrates from the fracture into the reservoir.

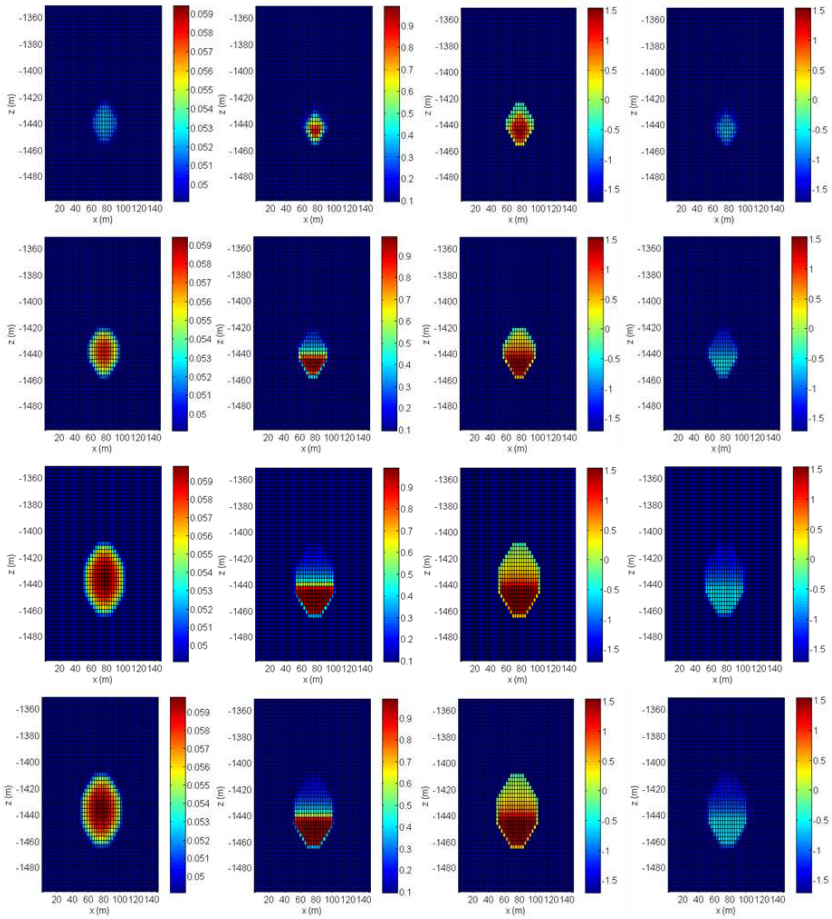

Figure 10: Cross-sectional view (x-z plane at the first y layer, stimulated zone) of reservoir models and resultant electrical conductivity models. The 1st column and the 2nd column show changes in porosity and fluid saturation values over time, respectively. The 3rd column shows changes in conductivity values when the electrically-engineered high-conductivity fluid (10,000 S/m) is injected. The 4th column shows changes in conductivity values when the brine (3.33 S/m) is injected. At the top of the third column, the yellow vertical line segments indicate observation wells for the vertical crosswell EM configuration. Two yellow ⊗ indicates the positions of horizontal wells for the horizontal crosswell EM configuration. The color charts for the 1st and 2nd column are linear and those for the 3rd and 4th column are based on the common log.

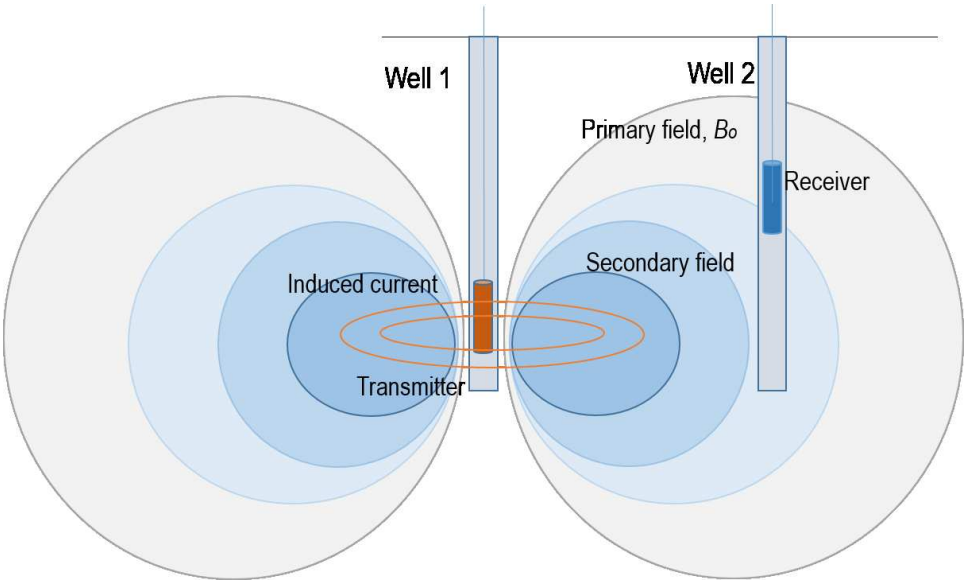

Figure 11: A typical crosswell EM survey configuration. Sources and receivers are lowered into the wells. The primary magnetic fields of the transmitter coil induce the electrical current. The current produces the secondary magnetic fields. The receivers record the both primary and magnetic fields.

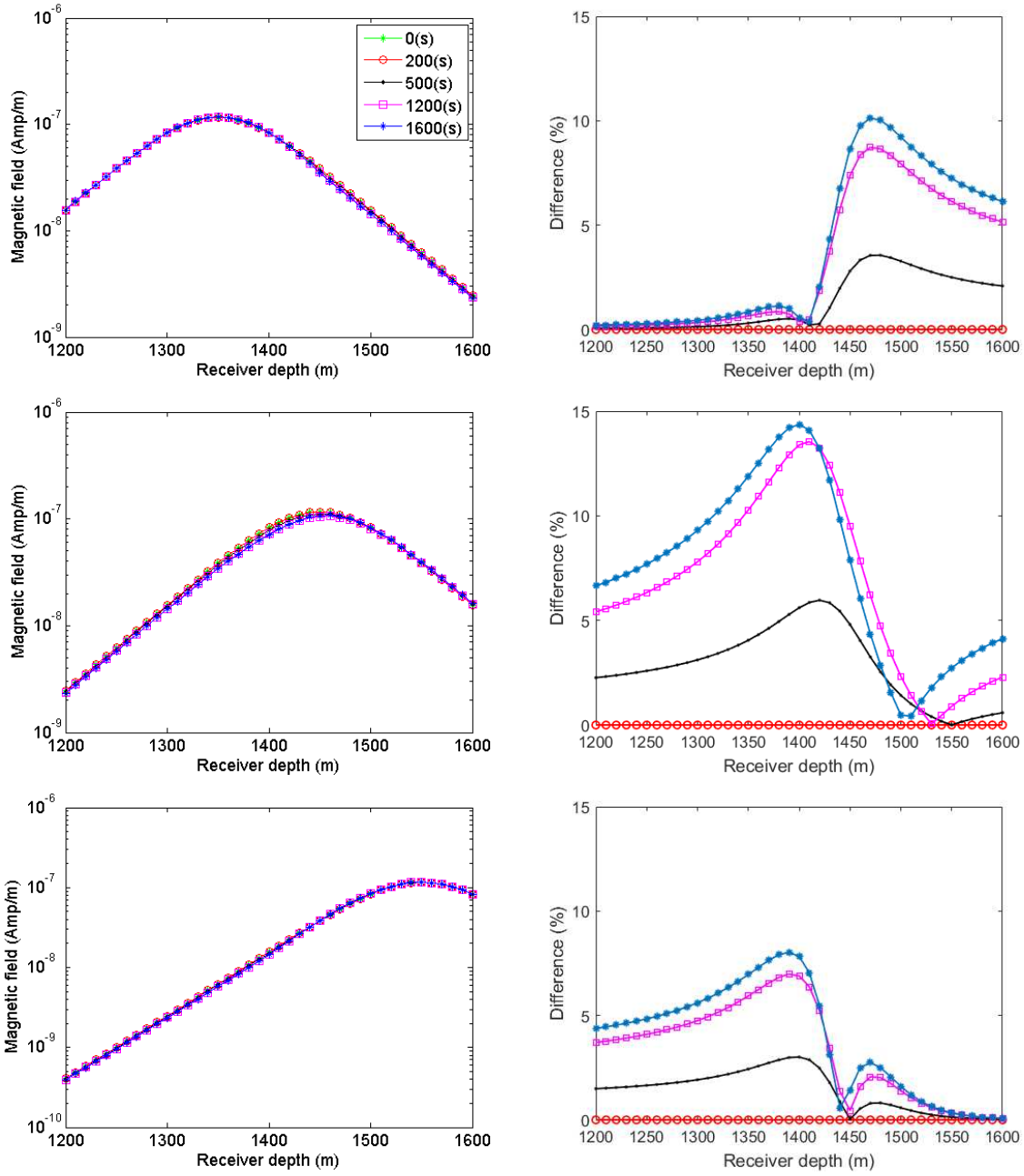

Figure 12: Magnetic field amplitudes (the left column) and their relative difference (the right column) with respect to the background magnetic field when the vertical crosswell configuration is applied to the conductivity model shown in the third column of Figure 10. Receivers are placed along the axis that is parallel to the z-axis and passes through the point (x=130 m and y=0 m).

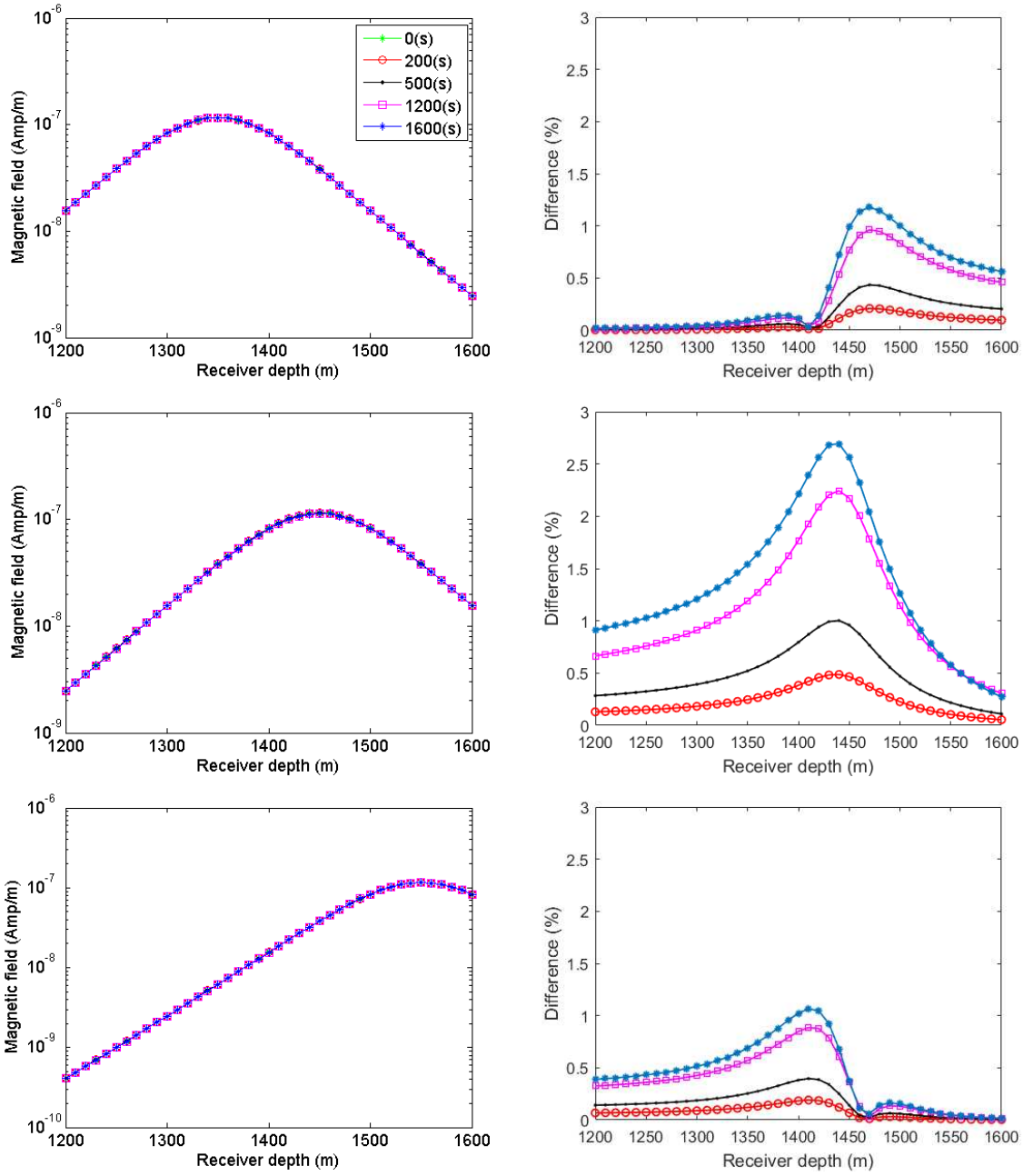

Figure 13: Magnetic field amplitudes (the left column) and their relative difference (the right column) with respect to the background magnetic field when the vertical crosswell configuration is applied to the conductivity model shown in the fourth column of Figure 10. Receivers are placed along the axis that is parallel to the z-axis and passes through the point (x=130 m and y=0 m).

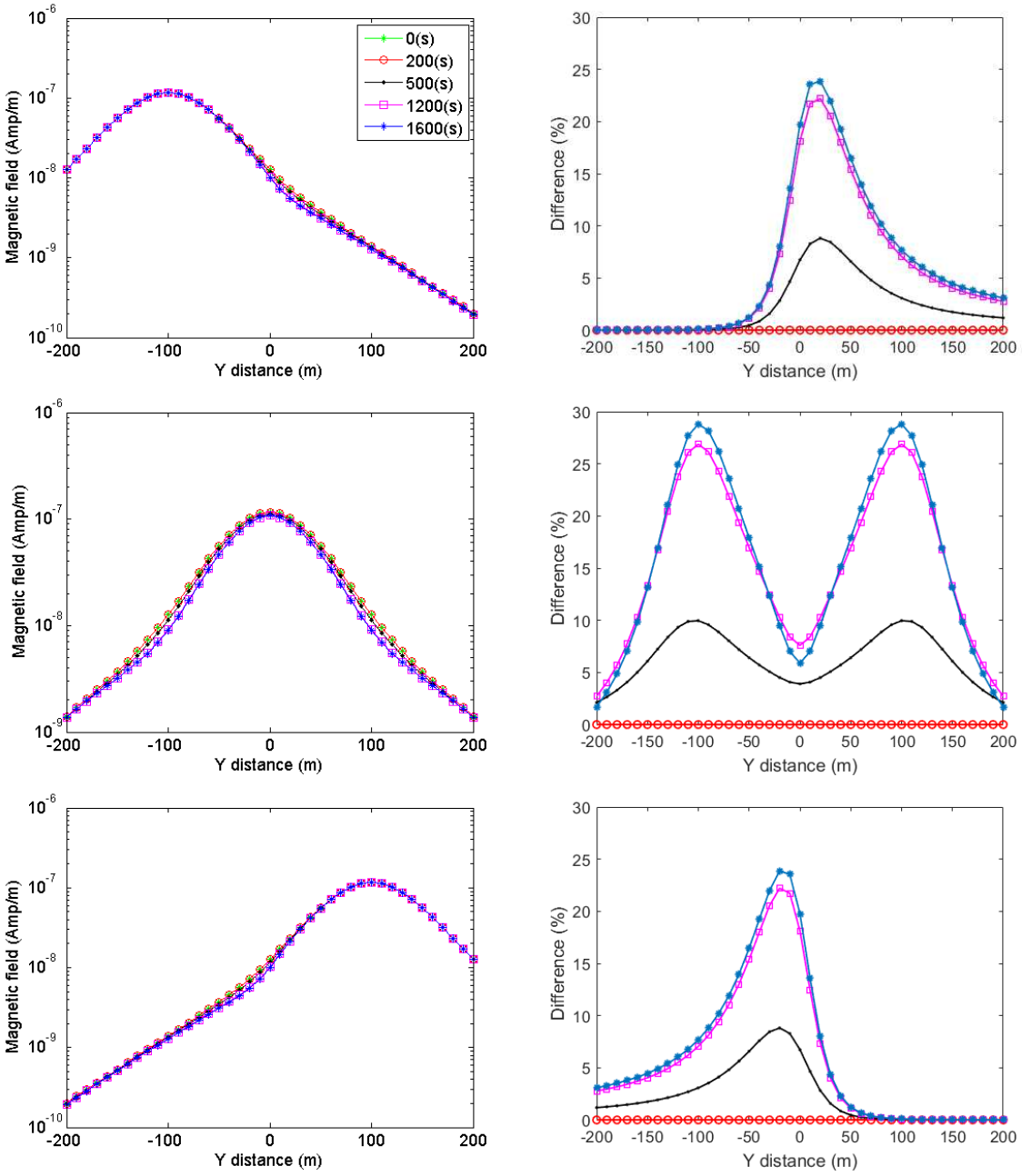

Figure 14: Magnetic field amplitudes (the left column) and their relative difference (the right column) with respect to the background magnetic field when the horizontal crosswell configuration is applied to the conductivity model shown in the third column of Figure 10. Receivers are placed along the axis that is parallel to the y-axis and passes through the point (x=130 m and z=-1440 m).

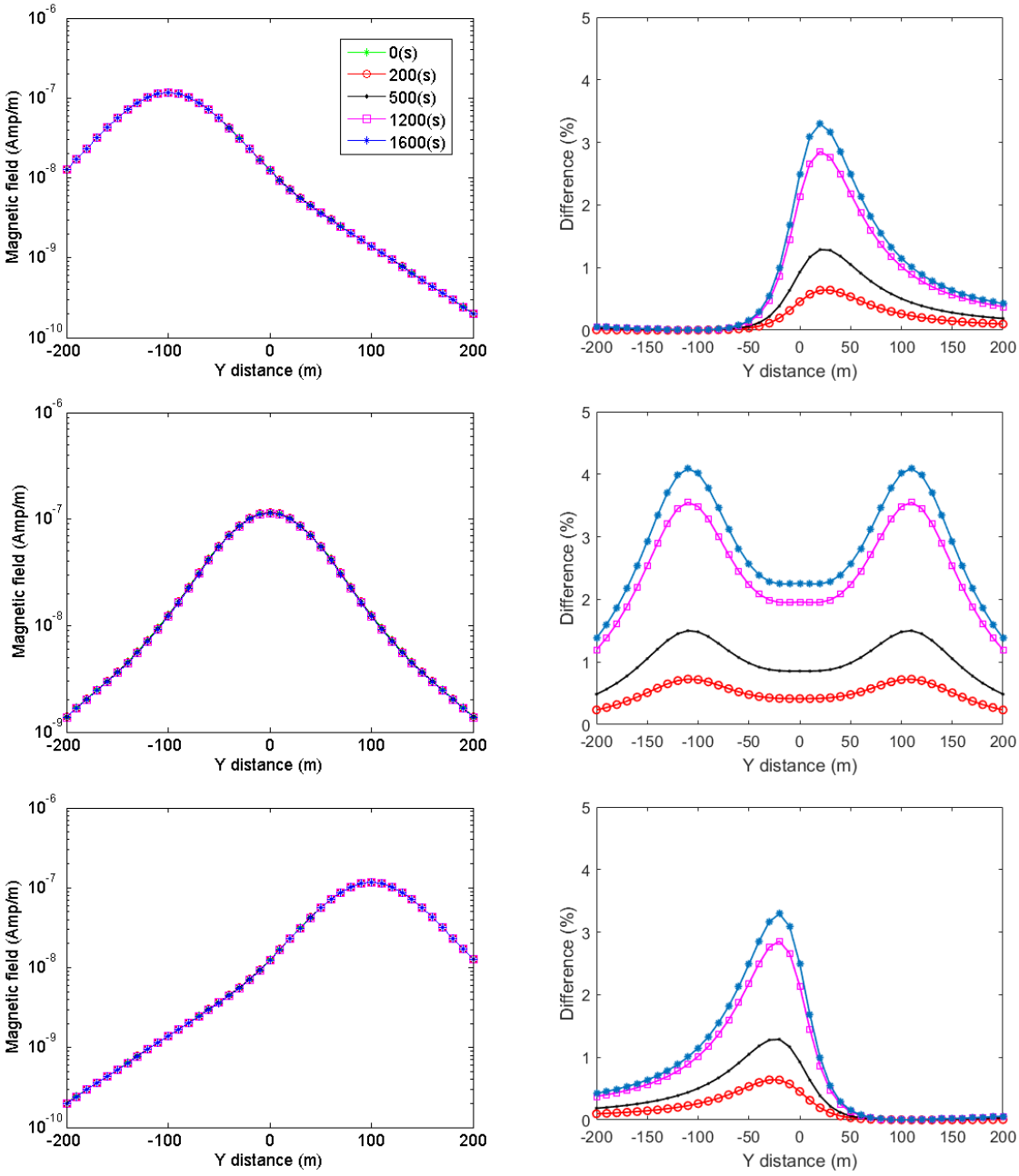

Figure 15: Magnetic field amplitudes (the left column) and their relative difference (the right column) with respect to the background magnetic field when the horizontal crosswell configuration is applied to the conductivity model shown in the fourth column of Figure 10. Receivers are placed along the axis that is parallel to the y-axis and passes through the point (x=130 m and z=-1440 m).